molecules

Article

Rationally Designed $Bi_2M_2O_9$ (M = Mo/W) Photocatalysts with Significantly Enhanced Photocatalytic Activity

Fangzhi Wang [1], Xiaoyan Zhou [1], Jing Li [1], Qiuyue He [1], Ling Zheng [1], Qing Liu [1], Yan Chen [1], Guizhai Zhang [1], Xintong Liu [2,*] and Hongda Li [3,*]

[1] School of Resources and Environmental Engineering, Shandong Agriculture and Engineering University, Jinan 250100, China; wfz0814@126.com (F.W.); yaling110@163.com (X.Z.); ripplelj@126.com (J.L.); ajheqiuyue@163.com (Q.H.); zhengl1988@126.com (L.Z.); liuqingliuqing2021@163.com (Q.L.); ychen0612@163.com (Y.C.); zgzok2005@163.com (G.Z.)
[2] School of Light Industry, Beijing Technology and Business University, Beijing 100048, China
[3] School of Microelectronics and Materials Engineering, Guangxi University of Science and Technology, Liuzhou 545006, China
* Correspondence: liuxt@btbu.edu.cn (X.L.); hdli@gxust.edu.cn (H.L.)

Abstract: Novel $Bi_2W_2O_9$ and $Bi_2Mo_2O_9$ with irregular polyhedron structure were successfully synthesized by a hydrothermal method. Compared to ordinary Bi_2WO_6 and Bi_2MoO_6, the modified structure of $Bi_2W_2O_9$ and $Bi_2Mo_2O_9$ were observed, which led to an enhancement of photocatalytic performance. To investigate the possible mechanism of enhancing photocatalytic efficiency, the crystal structure, morphology, elemental composition, and optical properties of Bi_2WO_6, Bi_2MO_6, $Bi_2W_2O_9$, and $Bi_2Mo_2O_9$ were examined. UV-Vis diffuse reflectance spectroscopy revealed the visible-light absorption ability of Bi_2WO_6, Bi_2MO_6, $Bi_2W_2O_9$, and $Bi_2Mo_2O_9$. Photoluminescence (PL) and photocurrent indicated that $Bi_2W_2O_9$ and $Bi_2Mo_2O_9$ pose an enhanced ability of photogenerated electron–hole pairs separation. Radical trapping experiments revealed that photogenerated holes and superoxide radicals were the main active species. It can be conjectured that the promoted photocatalytic performance related to the modified structure, and a possible mechanism was discussed in detail.

Keywords: $Bi_2W_2O_9$; $Bi_2Mo_2O_9$; modified structure; visible light; photocatalysis

check for updates

Citation: Wang, F.; Zhou, X.; Li, J.; He, Q.; Zheng, L.; Liu, Q.; Chen, Y.; Zhang, G.; Liu, X.; Li, H. Rationally Designed $Bi_2M_2O_9$ (M = Mo/W) Photocatalysts with Significantly Enhanced Photocatalytic Activity. *Molecules* **2021**, *26*, 7334. https://doi.org/10.3390/molecules26237334

Academic Editor: Vladimir K. Ivanov

Received: 16 November 2021
Accepted: 1 December 2021
Published: 2 December 2021

1. Introduction

Semiconductor photocatalysis technology has received increasing attention as a green approach since it can be widely applied in the areas of carbon dioxide reduction, water splitting, and organic pollutants degradation [1–4]. It is no doubt that TiO_2 is a popular photocatalyst. However, the band gap of TiO_2 is so wide that it can only respond to ultraviolet (UV) light. Therefore, tremendous efforts have been made to develop new visible-light-driven (VLD) photocatalysts, such as Bi_2WO_6, Bi_2MoO_6, MoS_2, g-C_3N_4, BiOBr, $BiVO_4$, and so on [5–8].

Both Bi_2WO_6 and Bi_2MoO_6 are active members of the Aurivillius oxide family with a special layer structure [9–12]. Bi_2WO_6 and Bi_2MoO_6 (Bi_2MO_6, M = W/Mo) possess similar crystal structure. Bi_2WO_6 consists of WO_6 layers and $[Bi_2O_2]^{2+}$ layers, and Bi_2MoO_6 consists of $[MoO_2]^{2+}$ layers and $[Bi_2O_2]^{2+}$ layers. Such a layered structure is favorable to the separation and transfer of photogenerated carriers [13]. Moreover, Bi_2MO_6 can absorb visible light and has good stability against photocorrosion. Thus, they have displayed potential photocatalytic performance for the decontamination of contaminants [14,15]. However, their practical application remains limited because of the high recombination rate of photogenerated electron–hole pairs in photocatalytic processes, and the visible-light use efficiency is still limited, which only responds to the light under 500 nm [16,17]. To solve these issues, composite materials with a heterojunction structure, doping of other ions, and loading of noble metal co-catalysts have been extensively investigated [18–22]. The results indicate that these methods essentially changed the structure of Bi_2MO_6 crystal to effectively inhibit the recombination of photogenerated electron–hole pairs under charge transmission, resulting in high photocatalytic performance. In this case, finding a kind of bismuthate with appropriate crystal structure is a potential approach to promote photocatalytic performance. Based on the special layer structure of Bi_2MO_6, a train of thought to modify the layer structure can be attempted.

The designation of $Bi_2M_2O_9$ (M = W/Mo) was adopted because of the similar crystal structure between $Bi_2W_2O_9$ and $Bi_2Mo_2O_9$. There are similarities and differences between $Bi_2M_2O_9$ and Bi_2MO_6. Both $Bi_2M_2O_9$ and Bi_2MO_6 consist of $(Bi_2O_2)^{2+}$ and $(M_xO_y)^{2-}$ (M = W/Mo) layers, while the difference is that the $(M_xO_y)^{2-}$ (M = W/Mo) layer is $(M_2O_7)^{2-}$ in $Bi_2M_2O_9$ and $(MO_4)^{2-}$ in Bi_2MO_6. Given this kind of difference, a sort of structure modification phenomenon can take place in $Bi_2M_2O_9$ crystal, and certainly lead to chemical bond changes.

In this study, novel morphology $Bi_2M_2O_9$ photocatalysts and ordinary Bi_2MO_6 were synthesized by a hydrothermal process. The modified structure of $Bi_2M_2O_9$ can facilitate charge separation to promote photocatalytic performance. Moreover, the modification of structure and chemical bond changes were studied, and the relationship between modified structure and promoted photocatalytic performance was investigated. We hope to explore a potential strategy to obtain a highly efficient visible-light-driven photocatalyst.

2. Result and Discussion

2.1. XRD Analysis

The typical diffraction patterns of the as-prepared samples can be observed in Figure 1, which indicates the successful synthesis of samples using the hydrothermal method. It also reveals the crystal style and major diffraction peaks of Bi_2WO_6, Bi_2MO_6, $Bi_2W_2O_9$, and $Bi_2Mo_2O_9$ in panel A to D, respectively. The major diffraction peaks at 2θ values of 27.5°, 33.4°, and 47.1° were indexed to (0 0 2), (6 0 0) and (0 2 0) of Bi_2WO_6 in Figure 1A, 2θ values of 27.7°, 29.9°, and 55.7° were indexed to (1 1 4), (1 1 5), and (1 3 4) of $Bi_2W_2O_9$ in Figure 1B, 2θ values of 10.9°, 28.3°, 33.1°, 47.2°, and 56.2° were indexed to (0 2 0), (1 3 1), (0 6 0), (0 6 2), and (1 9 1) of Bi_2MoO_6 in Figure 1C, and 2θ values of 25.8°, 31.8°, 36.9°, and 54.3° were indexed to (031), (330), (332) and (361) of $Bi_2Mo_2O_9$ in Figure 1D, respectively [23–25]. No signal for any crystalline phase of bismuth oxides were observed in the as-prepared photocatalysts.

It was reported that the crystal structure of Bi_2MO_6 and $Bi_2M_2O_9$ photocatalysts can be described as $(Bi_2O_2)^{2+}$ layer and $(MO_4)^{2-}$ or $(M_2O_7)^{2-}$ layer alternately connect to each other [26,27]. The polyhedron style model of Bi_2WO_6 and $Bi_2W_2O_9$ were exhibited in Figure 2. As shown in Figure 2A, there is a double W-O layer between two $(Bi_2O_2)^{2+}$ layers. The W atom and six surrounding oxygen atoms formed a WO_6 octahedra, which connects with other similar octahedra by axial O3 in a lengthways direction and equatorial O4, O5, O7 and O8 oxygen atoms in a crosswise direction, forming double $(W_2O_7)^{2-}$ layers. Top and bottom oxygen atoms O6 and O9 are located close to $(Bi_2O_2)^{2+}$ layers above and below WO_6 octahedra respectively, which eventually formed $Bi_2W_2O_9$ consisting of $(W_2O_7)^{2-}$ and $(Bi_2O_2)^{2+}$ layers. In addition, as-prepared $Bi_2W_2O_9$ structure can be regarded as a modification of the tetragonal structure. The formation principle of Bi_2WO_6 (Figure 2B) is similar to that of $Bi_2W_2O_9$. The WO_6 octahedra join another octahedra by axial O3 in a lengthways direction forming a single $(WO_4)^{2-}$ layer, and equatorial O5, O6, and O2 no longer join other WO_6 octahedra but join $(Bi_2O_2)^{2+}$ instead. Bi_2WO_6 with a single $(WO_4)^{2-}$ layer is formed in this way.

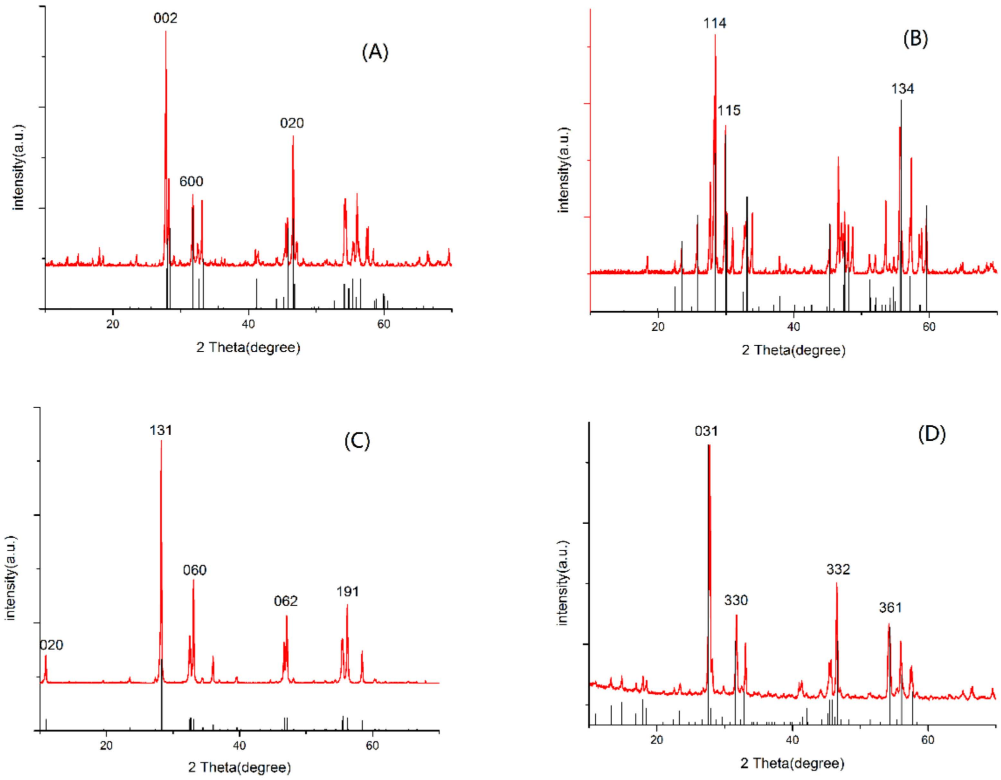

Figure 1. X-ray diffraction patterns of prepared samples (**A**) Bi_2WO_6, (**B**) $Bi_2W_2O_9$, (**C**) Bi_2MoO_6, and (**D**) $Bi_2Mo_2O_9$.

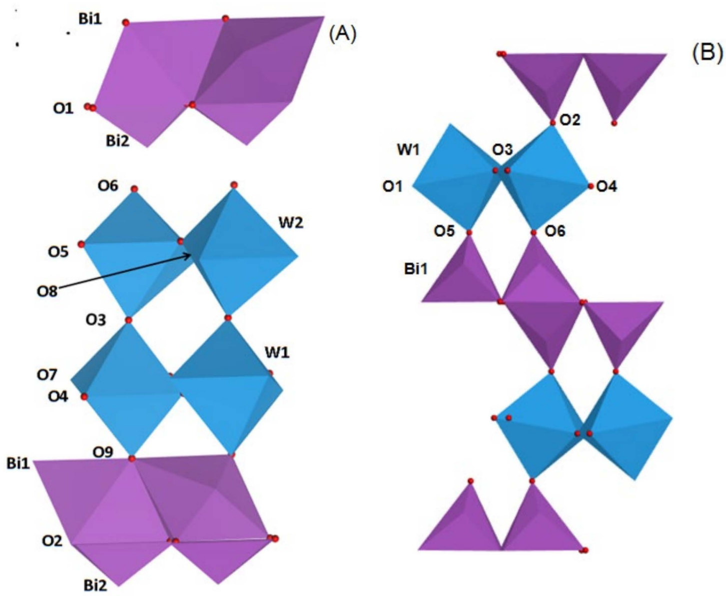

Figure 2. Models of $Bi_2W_2O_9$ (**A**) and Bi_2WO_6 (**B**) consist of $(Bi_2O_2)^{2+}$ and $(W_2O_7)^{2-}$ or $(WO_4)^{2-}$ layers.

As a result of the layer structure of Bi_2WO_6 and $Bi_2W_2O_9$, some translational motions of layered crystal can be regarded as a Rigid Unit (RU) layer motion. There are two shared RU modes in $Bi_2W_2O_9$, and the adjacent layers move parallel to the layer planes, which leads to modified compressional RU modes between adjacent layers in the perpendicular direction of the layer planes. As for Bi_2WO_6 structure, there is only one RU mode and the effect of compression between adjacent layers is weaker than that of $Bi_2W_2O_9$. As a result, compression of $Bi_2W_2O_9$ layer structure changes the chemical bond properties.

2.2. Morphology Characterization

SEM images of Bi_2WO_6, $Bi_2W_2O_9$, Bi_2MoO_6, and $Bi_2Mo_2O_9$ are illustrated in Figure 3 panels a to d, respectively. The morphology of Bi_2WO_6 in Figure 3A exhibits fastener-like nanoparticles with the radius of no more than 100 nm. The dimerization bismuthate $Bi_2W_2O_9$ certainly kept a similar fastener-like morphology as that of Bi_2WO_6 (Figure 3B). However, it can be observed that a volume increase phenomenon exists in $Bi_2W_2O_9$ crystal, and the average radius rose to about 400 nm at the same plotting scale compared to Bi_2WO_6. In terms of Bi_2MoO_6 and $Bi_2Mo_2O_9$, Figure 3C,D represent the panoramic SEM images of Bi_2MoO_6 and $Bi_2Mo_2O_9$. Both Bi_2MoO_6 and $Bi_2Mo_2O_9$ are of irregular polyhedron morphology and the variation is that there is also an increase of radius in $Bi_2Mo_2O_9$ compared to Bi_2MoO_6, but the increasing rate is less than that of $Bi_2W_2O_9$ and Bi_2WO_6. Double RU of $Bi_2M_2O_9$ increase of the distance of adjacent $(Bi_2O_2)^{2+}$ layers may be the possible reason for the volume augment. The novel morphology observed in SEM images may be attributed to the introduction of AOT surfactant during the synthesis process.

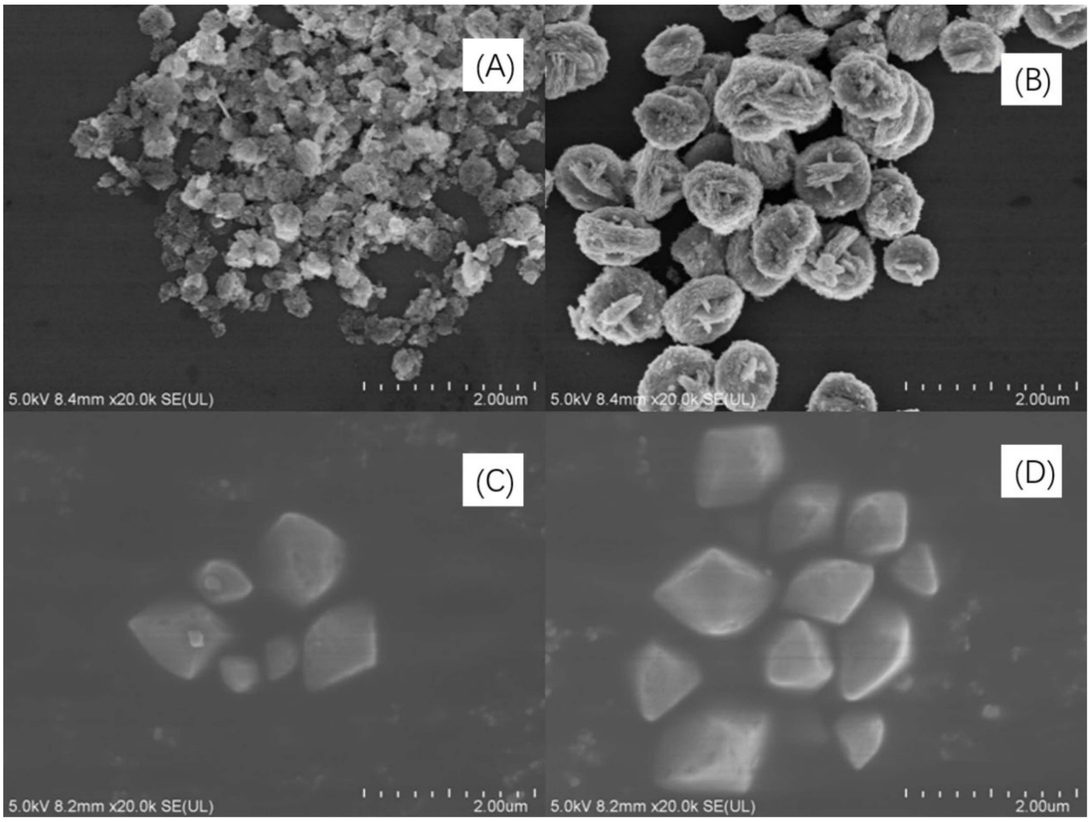

Figure 3. SEM images of (**A**) Bi_2WO_6, (**B**) $Bi_2W_2O_9$, (**C**) Bi_2MoO_6 and (**D**) $Bi_2Mo_2O_9$.

The possible synthesis mechanism is as follows. Raw materials have aggregated together to form some spheres during the hydrothermal process and finally the products have grown into clear-cut fastener-like or irregular polyhedron microspheres. At the beginning of the reaction, Bi^{3+} with $(M_xO_y)^{2-}$ ions precipitated quickly under the driving force of low-solubility products of $Bi_2M_xO_y$. Subsequently, AOT molecules are absorbed on the surface of nanoparticles through intermolecular interaction, and the newly formed nanoparticles are aggregated into loose microspheres, forming the $Bi_2M_xO_y$-AOT composite systems. These $Bi_2M_xO_y$-AOT composite systems connected with each other in various shapes. Finally, these amorphous nanoparticles underwent Ostwald ripening from the inside out as their surfaces come into contact with the surrounding solution. As a result, the internal nanoparticles tend to dissolve, which provides the driving force for spontaneous inside-out Ostwald ripening. This dissolution process could initiate at regions either near the surface or around the center of the microspheres. Redundant AOT was washed by the solution. Ostwald ripening occurred during the synthesis process of Bi_2WO_6, $Bi_2W_2O_9$, Bi_2MoO_6, and $Bi_2Mo_2O_9$ presumably depending on the packing of primary nanoparticles and ripening characteristics of AOT. A simple schematic illustration for the formation of the process is given in Figure 4.

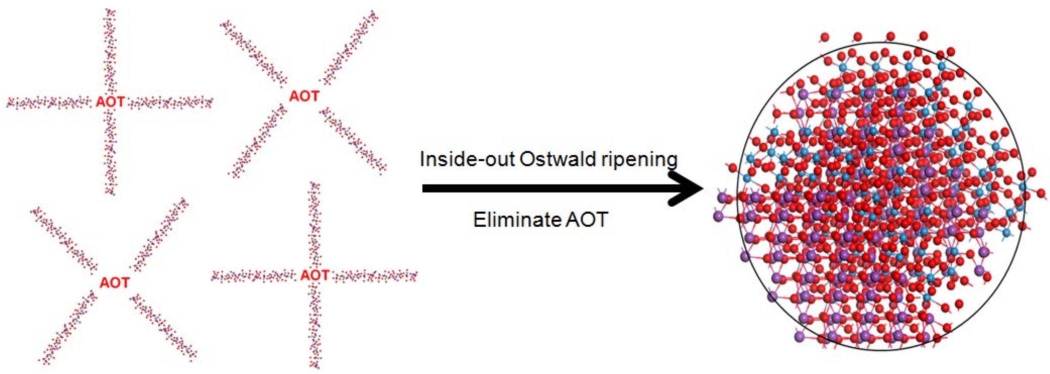

Figure 4. Possible formation process of novel morphology samples with AOT surfactant.

To confirm the atomic composition of Bi_2WO_6, $Bi_2W_2O_9$, Bi_2MoO_6, and $Bi_2Mo_2O_9$ samples conform to the theoretical value, EDX measurement was carried out and the data are listed in Table 1.

Table 1. EDX data of Bi_2WO_6, $Bi_2W_2O_9$, Bi_2MoO_6 and $Bi_2Mo_2O_9$.

Sample	Element	Wt%	At%
Bi_2WO_6	Bi	58.82	22.28
	W	27.90	12.02
	O	13.28	65.70
$Bi_2W_2O_9$	Bi	24.48	11.73
	W	24.32	13.25
	O	11.98	75.02
Bi_2MoO_6	Bi	67.66	21.56
	Mo	16.20	11.25
	O	16.14	67.19
$Bi_2Mo_2O_9$	Bi	54.13	14.62
	Mo	26.01	15.30
	O	19.86	70.07

The EDX data show that although there is deviation compared to the experimental data with theoretical value, the deviation is within acceptable limits.

2.3. Chemical State Analysis

X-ray photoelectron spectroscopy (XPS) analysis is used to further investigate the chemical state and surface chemical composition of Bi_2WO_6, $Bi_2W_2O_9$, Bi_2MoO_6, and $Bi_2Mo_2O_9$, especially to understand the structure modification effect of $Bi_2W_2O_9$ and $Bi_2Mo_2O_9$ on the binding energy, which has a great influence on photocatalytic performance [28].

The overall XPS spectra of Bi_2WO_6, $Bi_2W_2O_9$, Bi_2MoO_6, and $Bi_2Mo_2O_9$ are shown in Figure 5. The characteristic peaks of the Bi, W, Mo, and O elements were detected. Before the analysis, all peaks of the other elements were calibrated according to the deviation between the C 1*s* peak and the standard signal of C 1*s* at 284.8 eV [29]. No XPS characteristic peaks of N 1*s* were detected at around 400 eV, although raw material contained nitrogen, which indicated no nitrogen was doped in Bi_2WO_6, $Bi_2W_2O_9$, Bi_2MoO_6, and $Bi_2Mo_2O_9$ samples. The signals of Bi_2WO_6 in Figure 5B were attributed to Bi $4f_{7/2}$ and Bi $4f_{5/2}$ states respectively at 159.2 and 164.5 eV [30]. The binding energy of W $4f_{7/2}$ and W $4f_{5/2}$ were observed at 35.4 and 37.6 eV (Figure 5C) that can be attributed to W^{6+} [31]. The binding energy peak in Figure 5D located at 530.0 eV corresponds to O 1*s* state in Bi_2WO_6 [32]. The same examined element spectra in $Bi_2W_2O_9$ were exhibited together with those in Bi_2WO_6 in the same panels. It can be obviously observed that all Bi, W, and O have similar peak patterns, and the difference is that characteristic peaks of $Bi_2W_2O_9$ shift towards higher binding energy, which illustrates that the chemical environment has changed, and a higher binding energy indicates the existence of the electron-drawing group. The same phenomenon can be observed in Bi_2MoO_6 and $Bi_2Mo_2O_9$ in panels E to H, where Bi, Mo, and O elements in $Bi_2Mo_2O_9$ pose a higher binding energy.

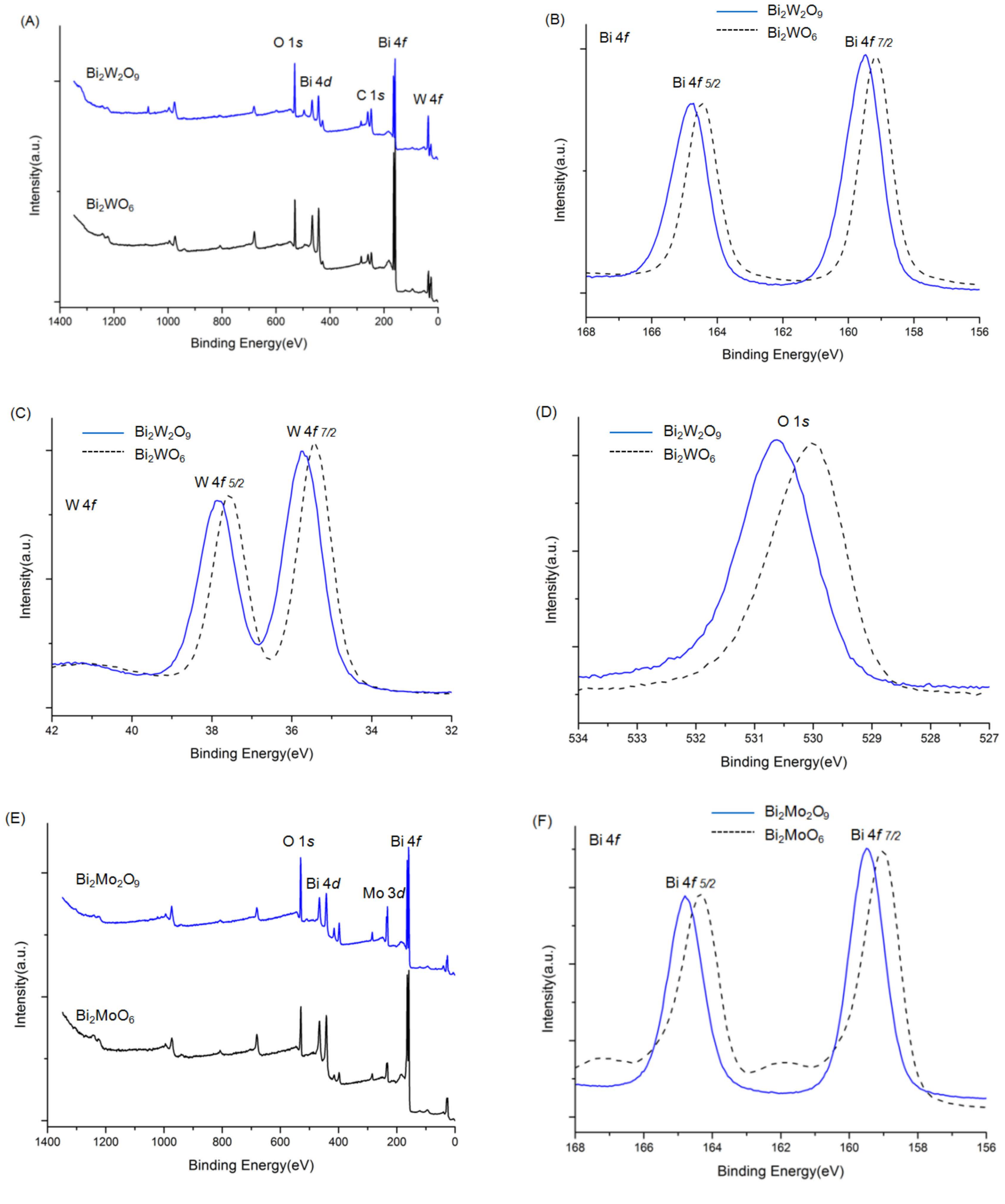

Figure 5. *Cont.*

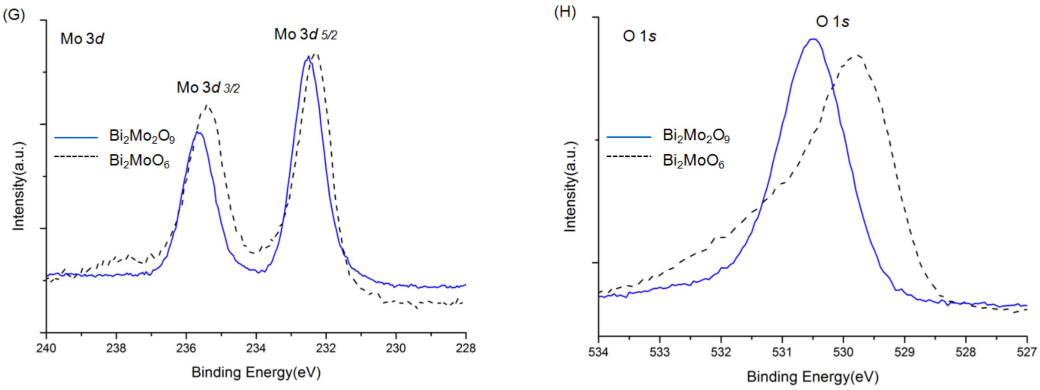

Figure 5. XPS spectra of Bi_2WO_6, $Bi_2W_2O_9$, Bi_2MoO_6 and $Bi_2Mo_2O_9$: ((**A**): Bi_2WO_6 and $Bi_2W_2O_9$) ((**E**): $Bi_2W_2O_9$) overall spectra; (**B**,**F**) Bi 4*f*; (**C**) W *f*; (**D**,**H**) O 1*s*; (**G**) Mo 3*d*.

2.4. Optical Properties

The optical properties of Bi_2WO_6, $Bi_2W_2O_9$, Bi_2MoO_6, and $Bi_2Mo_2O_9$ were characterized through a UV-Vis diffuse reflectance spectrometer in the wavelength range of 250–800 nm [33]. Compared to Bi_2WO_6 and Bi_2MoO_6, it can be observed obviously that there is a red shift of the light absorption edge from $Bi_2W_2O_9$ and $Bi_2Mo_2O_9$ samples, respectively. The optical band gap of the as-prepared photocatalysts was calculated using the following Equation (1) [34].

$$A h\nu = \alpha(h\nu - E_g)^{n/2} \tag{1}$$

in which h, α, A, ν, and E_g represent Planck's constant with the unit of eV, a constant, the absorption coefficient near the absorption edge, light frequency, the absorption band gap energy, respectively, and n is equal to 1 or 4, depending on whether the optical transition type is direct or indirect. Bi_2WO_6, $Bi_2W_2O_9$, Bi_2MoO_6, and $Bi_2Mo_2O_9$ have a direct band gap, and n is 1 herein. The inset shows the curve of $(\alpha h\nu)^2$ versus hν for the as-prepared samples. It can be observed that an evidential red shift exists in $Bi_2M_2O_9$ samples compared to Bi_2MO_6 and $Bi_2Mo_2O_9$ has the greatest absorption range (Figure 6). The band gap energy (E_g) of Bi_2WO_6, $Bi_2W_2O_9$, Bi_2MoO_6 and $Bi_2Mo_2O_9$ were computed to be 2.78, 2.76, 2.72, and 2.70 eV respectively and exhibit in the inset of Figure 6. The result indicated that $Bi_2M_2O_9$ samples presented an enhanced absorbance ability compared to Bi_2MO_6.

2.5. Photocatalytic Properties

The photocatalytic performance of the as-synthesized photocatalysts were evaluated by examining the photodegradation of MB solution under visible-light irradiation (Figure 7). Generally, the different concentrations of MB adsorbed on the catalyst surface will have a great influence on the photocatalytic performance, so the adsorption ratio was collected when adsorption–desorption equilibrium was achieved before irradiation [35]. Bi_2WO_6, $Bi_2W_2O_9$, Bi_2MoO_6, and $Bi_2Mo_2O_9$ samples presented a similar capacity for MB absorption, and it can be obviously observed that $Bi_2M_2O_9$ samples exhibit a higher photocatalytic activity than that of Bi_2MO_6. $Bi_2Mo_2O_9$ displayed the best photocatalytic activity among the four test samples, and the photodegradation rate reached up to 75% within 4 h.

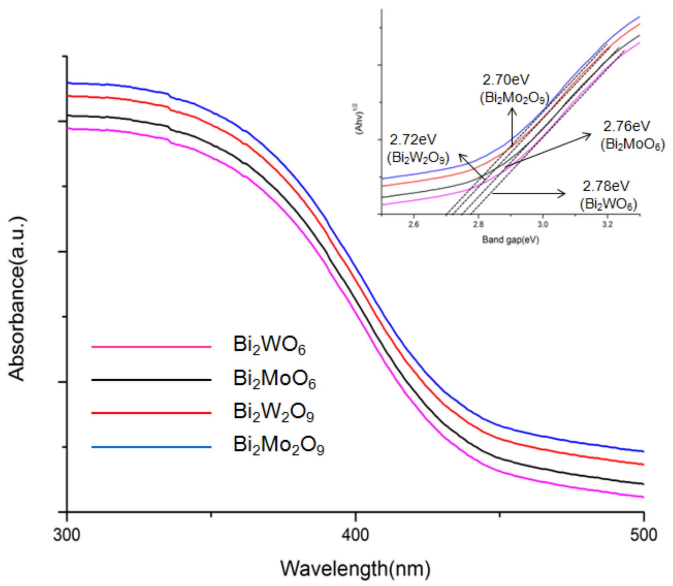

Figure 6. DRS spectra of Bi_2WO_6, $Bi_2W_2O_9$, Bi_2MoO_6 and $Bi_2Mo_2O_9$. The inset shows the band gap energies.

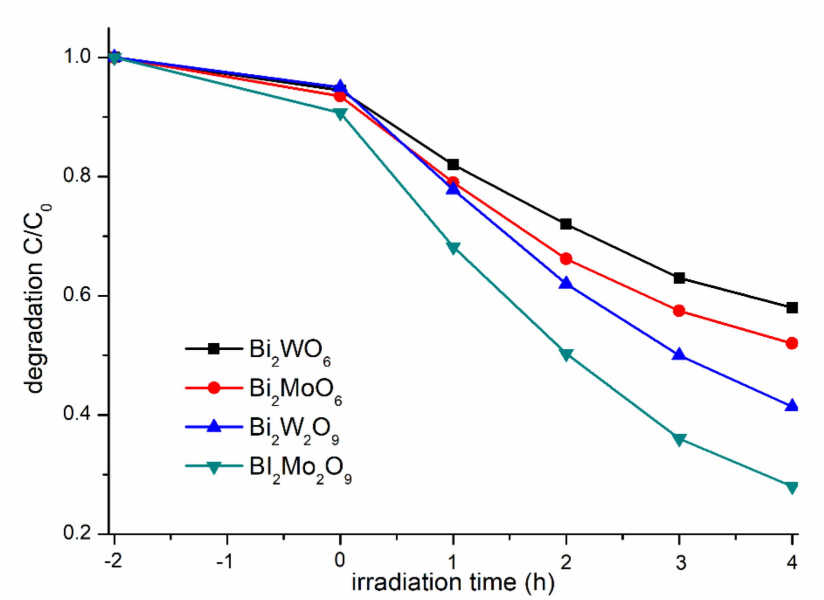

Figure 7. Comparison of absorption and degradation rate of MB using Bi_2WO_6, $Bi_2W_2O_9$, Bi_2MoO_6 and $Bi_2Mo_2O_9$.

In our work, the cycling experiment for MB photocatalytic degradation was performed under visible-light irradiation to evaluate the stability of the best photocatalyst ($Bi_2Mo_2O_9$). As shown in Figure 8, the photocatalytic performance of $Bi_2Mo_2O_9$ did not display any significant reduction for MB degradation. This result confirms that $Bi_2M_2O_9$ photocatalysts are not easily photo-corroded during the photodegradation of the pollutant molecules, which is important for their application.

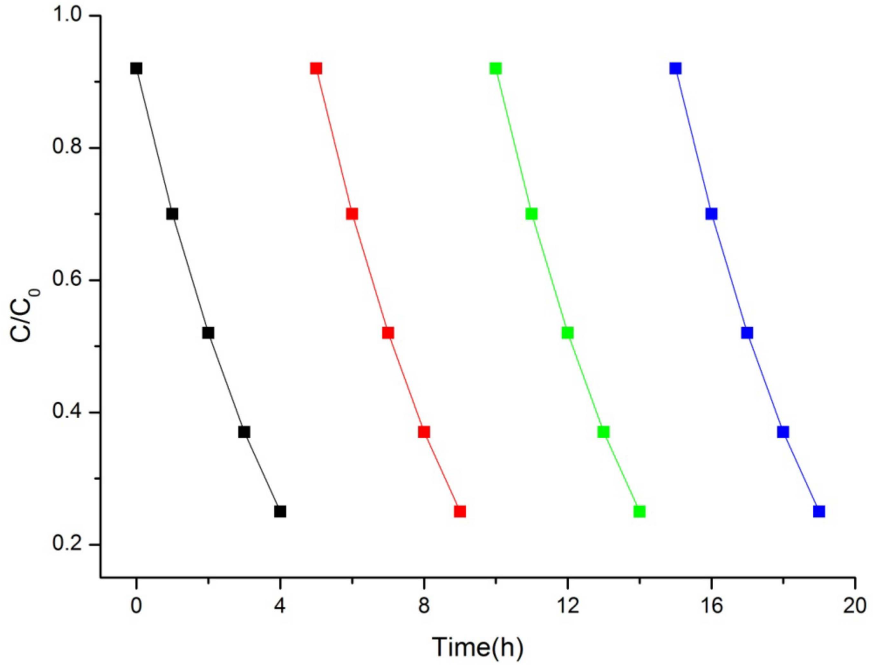

Figure 8. Cyclic photocatalytic activity of MB by $Bi_2Mo_2O_9$ photocatalyst.

2.6. Photocatalytic Mechanism

Overall, the photocatalytic activity of $Bi_2M_2O_9$ was highly improved compared to ordinary Bi_2MO_6. As noted above, such enhancement may partially come from structure modification. To understand the structure modification effect on $Bi_2M_2O_9$ and the charge behavior during the photocatalyst process, trapping experiments with different scavengers were performed with $Bi_2Mo_2O_9$ (Figure 9). In this way, active species could be determined, including holes (h^+), superoxide radicals ($^{\cdot}O_2^-$) and hydroxyl radicals ($^{\cdot}OH$) with effective oxidation and reduction potentials [36–38]. In the present study, isopropyl alcohol (IPA), ethylenediaminetetraacetic acid disodium salts (EDTA), and 1,4-benzoquinone (BQ) were used as scavengers of $^{\cdot}OH$, h^+, and $^{\cdot}O_2^-$, respectively. Remarkably, MB degradation was halted as we added the scavenger EDTA (1 mM) for h^+ to the reaction system. Meanwhile, the photodegradation rate of MB evidently declined with the addition of the scavenger BQ (1 mM) for $^{\cdot}O_2^-$. However, there was no clear reduction in the degradation rate of MB when the scavenger IPA (1 mM) for $^{\cdot}OH$ was added. These results indicate that h^+ and $^{\cdot}O_2^-$ were the main reactive species, while $^{\cdot}OH$ had little influence on the MB degradation process.

The electron–hole separation condition was tested by PL in the range of 400–700 nm. As shown in Figure 10, compared to Bi_2MO_6, the PL intensities of $Bi_2M_2O_9$ were perceptibly weaker, and $Bi_2Mo_2O_9$ has the lowest peak intensity. Usually, a lower PL intensity shows stronger photogenerated charge separation, which leads to excellent photocatalytic efficiency of the photocatalyst [39]. The experiment results reveal that $Bi_2M_2O_9$ has an elevated ability of electron–hole separation.

The photocurrent responses directly related to the generation and transfer of the photogenerated electrons and holes [40,41]. Figure 11 shows the photocurrent response of Bi_2WO_6, $Bi_2W_2O_9$, Bi_2MoO_6 and $Bi_2Mo_2O_9$ samples. Obviously, the current abruptly increased and decreased through on–off cycles under visible-light irradiation. $Bi_2M_2O_9$ samples showed a significantly improved photocurrent response compared to that of the Bi_2MO_6 samples. This suggests that more efficient separation of the photogenerated charge carriers occurred in $Bi_2M_2O_9$ samples. In addition, it should be noted that $Bi_2M_2O_9$ samples hold obvious residual currents when the light source is switched off. This is probably attributed to the modified structure; it may lead to some remnant electron–hole pairs when the visible-light source is removed, which could release the trapped electrons or holes because of the self-thermal motion.

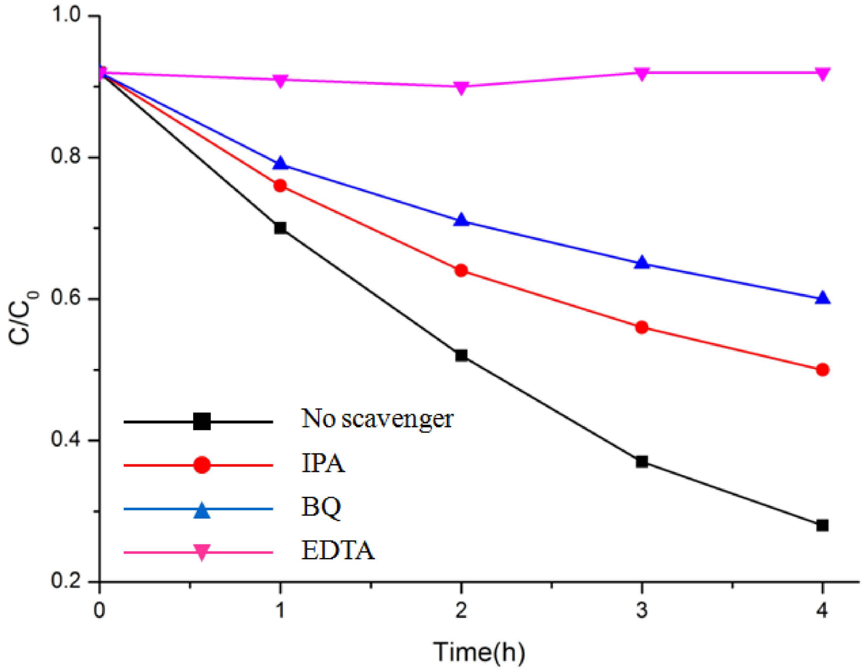

Figure 9. Photocatalytic degradation of MB over $Bi_2Mo_2O_9$ photocatalyst with the addition of scavengers EDTA, BQ, and IPA.

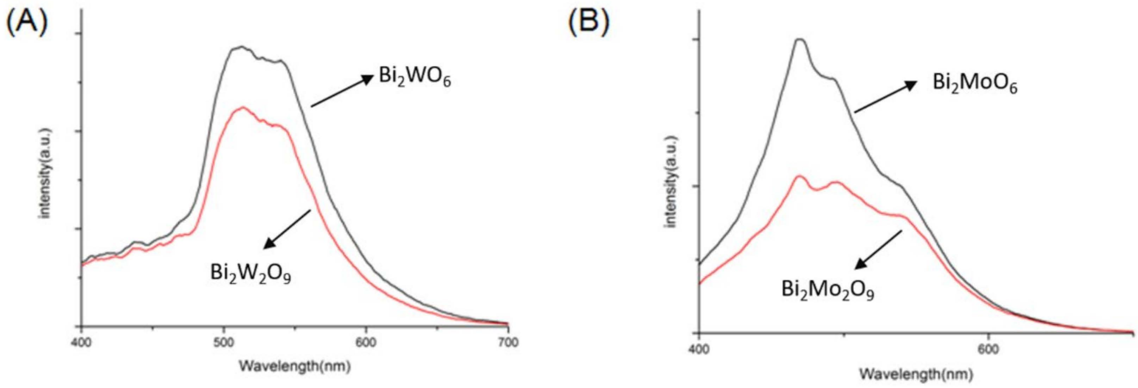

Figure 10. Photoluminescence (PL) spectra of (**A**) Bi_2WO_6 and $Bi_2W_2O_9$; (**B**) Bi_2MoO_6 and $Bi_2Mo_2O_9$.

Based on the characterization methods above, a possible photocatalytic mechanism of the $Bi_2M_2O_9$ photocatalyst under visible-light irradiation is therefore proposed, and the $Bi_2M_2O_9$ photocatalyst has a stable double Rigid Unit (RU), which consists of two octahedral layers. Double RU mode can be regarded as a strong electron-drawing group, and $Bi_2M_2O_9$ show a stable reduced bond distance of octahedral RU. The influence of modified structure is reflected in PL test and photocurrent measurement. The reduction of PL intensity and the enhancement of photocurrent express promoted photogenerated electron–hole pairs separation ability; the strong electron-drawing group traps the photogenerated electrons and leads to the increase of active species to promote the photocatalytic performance.

As shown in Figure 12, the photogenerated electrons could migrate to the conduction band (CB) from the valence band (VB) and the photogenerated holes formed in the valence band when the semiconductor was irradiated with visible light. The shortened bond distance of octahedral RU generates a strong electron-drawing efficiency that traps the electron firmly and reduces the recombination rate. Evidentially, the trapped electrons could easily transfer to the oxygen molecules (O_2) adsorbed on the surface of the $Bi_2M_2O_9$

catalysts. Subsequently, the released electrons react with O_2 to form the active superoxide radical anion species (O_2^-). The electron capture and release process enhances the charge transfer and separation efficiency of photogenerated electrons and holes, which contributes to organic contaminant photodegradation by the h^+ and $^{\cdot}O_2^-$ species.

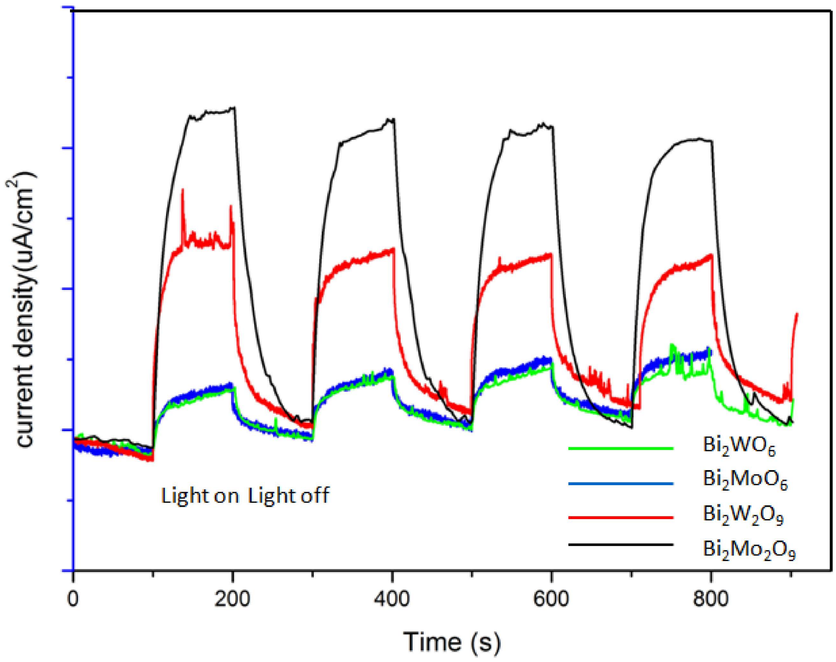

Figure 11. Photocurrent responses of Bi_2WO_6, $Bi_2W_2O_9$, Bi_2MoO_6 and $Bi_2Mo_2O_9$ samples under visible-light irradiation.

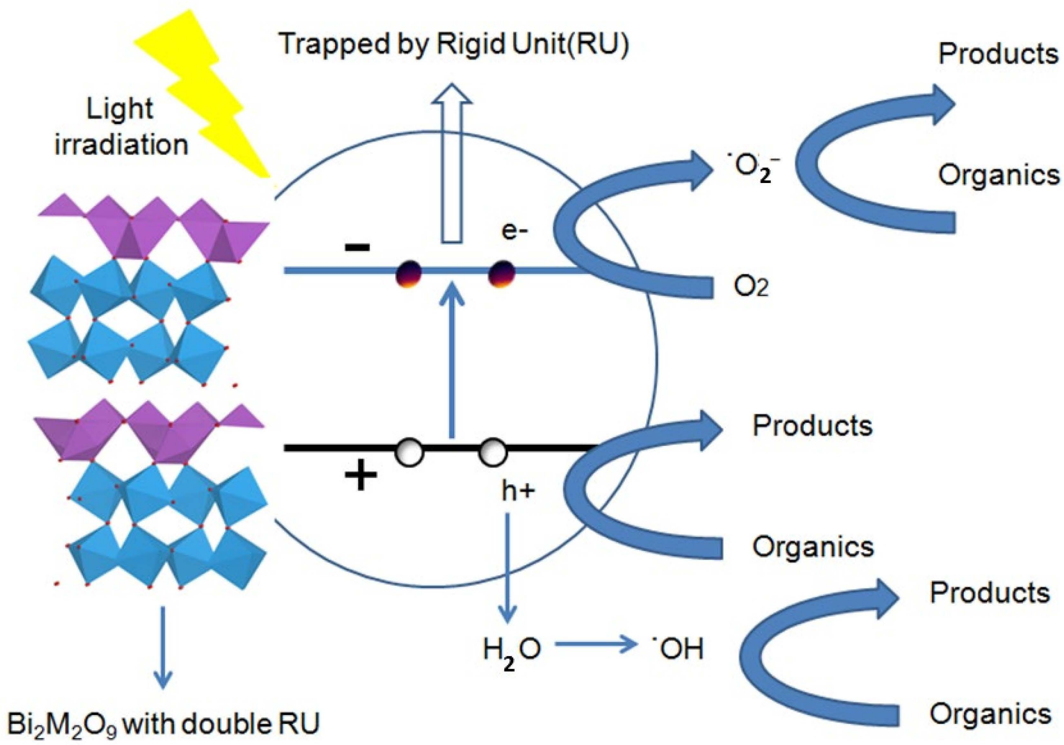

Figure 12. Schematic illustration of the mechanism of $Bi_2M_2O_9$ photocatalyst under visible-light irradiation.

Therefore, the above process indicates that an appropriate increase the number of $(Bi_2O_2)^{2+}$ layers and $(W_2O_7)^{2-}$ layers to form a stable Rigid Unit (RU) mode could significantly improve photocatalytic activity.

3. Experimental

3.1. Synthesis of the Photocatalysts

All the reagents used in this study were of analytical purity (Sinopharm Chemical Reagents Co., Ltd., Shanghai, China) and used without any further purification. Bi_2WO_6, $Bi_2W_2O_9$, Bi_2MoO_6 and $Bi_2Mo_2O_9$ photocatalysts were prepared through a hydrothermal method and the general synthesis processes were as follows: proportionate amounts of sodium tungstate ($Na_2WO_4{\cdot}H_2O$) or sodium molybdate ($Na_2MoO_4{\cdot}H_2O$) were dissolved in Milli-Q water. Then proportional bismuth (III) nitrate pentahydrate ($Bi(NO_3)_3{\cdot}5H_2O$) was dissolved in nitric acid and anionic surfactant AOT was introduced into the solution sequence under stirring to form a transparent solution and ensure Bi:Mo and Bi:W keeps 2:1 during the preparation process of Bi_2WO_6 and Bi_2MoO_6, similarly, a value of the ratio of Bi and W or Mo stays at 1 when preparing $Bi_2W_2O_9$ and $Bi_2Mo_2O_9$. We adjust the pH value of the solution to ca. 7 using NaOH solution. The slurry was stirred for another 30 min and then poured into Teflon-lined stainless steel autoclaves. The sealed reactors were then heated at 180 °C for 12 h. Then, the products were cooled to room temperature naturally and collected via centrifugation and washed in Milli-Q water and ethanol several times to make sure that the residual impurities were all removed, and then the product was dried at 80 °C for 8 h.

3.2. Characterization of the Photocatalysts

The crystalline phases of the as-prepared samples were analyzed using X-ray diffraction (XRD) (D/MAX-RB, Rigaku, Tokyo, Japan). The diffraction patterns were recorded in the 2θ range from 10 to 70° with a Cu Kα source (λ = 1.5418 Å) running at 40 KV and 30 mA. The morphology images of the as-prepared samples were captured using scanning electron microscopy (SEM) equipped with an energy-dispersive X-ray spectrometer (EDX) on a SUPRA 55 SAP-PHIRE instrument operating at 20 KV. High-resolution transmission electron microscopy (HRTEM) images were acquired with a transmission electron microscopy (F-20, FEI, Hillsboro, OR, USA) at an accelerating voltage of 200 KV. The UV-Vis diffuse reflectance spectra of the as-prepared samples were examined at room temperature using a UV-Vis spectrophotometer (T9s; Persee, Beijing, China) equipped with an integrating sphere. $BaSO_4$ was used as the blank reference. Photoluminescence (PL) spectra were recorded using a fluorescence spectrophotometer (F-4500; Hitachi, Tokyo, Japan) with a Xe lamp as the excitation light source. X-ray photoelectron spectroscopy (XPS) was examined on an X-ray photoelectron spectrometer (ESCALAB 250Xi, Thermo Scientific, Waltham, MA, USA) using an Al Kα radiation.

3.3. Photocatalytic Experiment

The photocatalytic activities of Bi_2WO_6, $Bi_2W_2O_9$, Bi_2MoO_6, and $Bi_2Mo_2O_9$ photocatalysts under visible light were assessed by degrading 10 mmol·L^{-1} methylene blue (MB). A 400 W Xe lamp with a UV-cut-off filter (λ > 420 nm) was used as a light source and set about 10 cm apart from the reactor. The experiments were as follows: 40 mg of the photocatalyst was dispersed in 40 mL of MB solution. It was then stirred for 120 min in the dark to achieve an adsorption–desorption equilibrium before light irradiation. During the irradiation, the reaction samples were collected at 60 min intervals and centrifuged to separate out the photocatalyst particles. The ratios (C/C_0) of the MB were adopted to evaluate the degradation efficiency (i.e., C_0 was the initial concentration, where C was the concentration at a certain time) by checking the absorbance spectrum at 664 nm for MB using a UV-Vis spectrophotometer (T9s; Persee, Beijing, China).

3.4. Measurement of Photocurrent

The measurement of the photocurrent was carried out with an electrochemical workstation (5060F, RST, Zhengzhou, China) in a standard three-electrode system including the samples, an Ag/AgCl electrode (saturated KCl), and a Pt filament used as the working electrode, reference electrode, and counter electrode, respectively. In addition, a pre-made 0.5 mol L^{-1} Na_2SO_4 aqueous solution was introduced as the electrolyte. A 100 W incandescent lamp with a 420 nm cut-off filter was used as the light source. The working electrode was manufactured as follows: 5 mg samples were appended to 2 mL of ethanol and Nafion mixture solution (v/v = 30:1), followed by spreading on the middle of an ITO glass in a rounded hole with a diameter of 6 mm.

4. Conclusions

In this study, ordinary Bi_2WO_6 and Bi_2MoO_6 samples were successfully synthesized; furthermore, a novel $Bi_2Mo_2O_9$ fastener sphere and a $Bi_2W_2O_9$ irregular polyhedron were prepared by a hydrothermal method with AOT introduced. The results revealed that structure-modified $Bi_2W_2O_9$ and $Bi_2Mo_2O_9$ exhibited enhanced photocatalytic performance. The Rigid Unit (RU) and modified bond structure influence the trapping–release process of electrons to promote the separation efficiency of photogenerated electron–hole pairs. Therefore, an appropriate increase of the layer number of $(W_2O_7)^{2-}$ or $(Mo_2O_7)^{2-}$ between $(Bi_2O_2)^{2+}$ layers to form an RU strong electron-drawing group as a method of structure modification can be a potential strategy to improve visible-light photocatalytic activity by affecting the charge behavior.

Author Contributions: Conceptualization, F.W., X.L. and H.L.; methodology, G.Z.; validation, Y.C., H.L.; formal analysis, J.L.; investigation, L.Z., Q.L.; data curation, X.Z., Q.H.; writing—review and editing, F.W., X.L. All authors have read and agreed to the published version of the manuscript.

Funding: This research was funded by the Inspiration Fund of Shandong Agriculture and Engineering University (Grant No. BSQJ201811), Qingchuang Science and Technology Program of Shandong Province in China (grant no. 2019KJF029), and the National Natural Science Foundation of China (Grant No. 61801274).

Institutional Review Board Statement: Not applicable.

Informed Consent Statement: Not applicable.

Data Availability Statement: The data presented in the study are available from the corresponding author.

Conflicts of Interest: The authors declare no conflict of interest.

Sample Availability: Samples of the compounds are not available from the authors.

References

1. Xu, C.; Anusuyadevi, P.R.; Aymonier, C.; Luque, R.; Marre, S. Nanostructured materials for photocatalysis. *Chem. Soc. Rev.* **2019**, *48*, 3868–3902. [CrossRef] [PubMed]
2. Wei, Z.; Liu, J.; Shangguan, W. A review on photocatalysis in antibiotic wastewater: Pollutant degradation and hydrogen production. *Chin. J. Catal.* **2020**, *41*, 1440–1450. [CrossRef]
3. Asadzadeh-Khaneghah, S.; Habibi-Yangjeh, A. g-C_3N_4/carbon dot-based nanocomposites serve as efficacious photocatalysts for environmental purification and energy generation: A review. *J. Clean. Prod.* **2020**, *276*, 124319. [CrossRef]
4. Bie, C.; Yu, H.; Cheng, B.; Ho, W.; Fan, J.; Yu, J. Design, Fabrication, and Mechanism of Nitrogen-Doped Graphene-Based Photocatalyst. *Adv. Mater.* **2021**, *33*, 2003521. [CrossRef]
5. Liu, X.; Gu, S.; Zhao, Y.; Zhou, G.; Li, W. $BiVO_4$, Bi_2WO_6 and Bi_2MoO_6 photocatalysis: A brief review. *J. Mater. Sci. Technol.* **2020**, *56*, 45–68. [CrossRef]
6. Wang, F.; Li, W.; Gu, S.; Li, H.; Wu, X.; Liu, X. Samarium and Nitrogen Co-Doped Bi_2WO_6 Photocatalysts: Synergistic Effect of $Sm3^{+}/Sm^{2+}$ Redox Centers and N-Doped Level for Enhancing Visible-Light Photocatalytic Activity. *Chem.-Eur. J.* **2016**, *22*, 12859–12867. [CrossRef]
7. Zhang, J.; Zhu, Z.; Jiang, J.; Li, H. Synthesis of Novel Ternary Dual Z-scheme AgBr/$LaNiO_3$/g-C_3N_4 Composite with Boosted Visible-Light Photodegradation of Norfloxacin. *Molecules* **2020**, *25*, 3706. [CrossRef] [PubMed]

8. Mishra, A.; Mehta, A.; Basu, S.; Shetti, N.P.; Reddy, K.R.; Aminabhavi, T.M. Graphitic carbon nitride (g–C_3N_4)–based metal-free photocatalysts for water splitting: A review. *Carbon* **2019**, *149*, 693–721. [CrossRef]
9. Li, H.; Li, W.; Gu, S.; Wang, F.; Zhou, H. In-built Tb^{4+}/Tb^{3+} redox centers in terbium-doped bismuth molybdate nanograss for enhanced photocatalytic activity. *Catal. Sci. Technol.* **2016**, *6*, 3510–3519. [CrossRef]
10. Yuan, Y.J.; Shen, Z.; Wu, S.; Su, Y.; Pei, L.; Ji, Z.; Ding, M.; Bai, W.; Chen, Y.; Yu, Z.T.; et al. Liquid exfoliation of g-C_3N_4 nanosheets to construct 2D-2D MoS_2/g-C_3N_4 photocatalyst for enhanced photocatalytic H_2 production activity. *Appl. Catal. B-Environ.* **2019**, *246*, 120–128. [CrossRef]
11. Li, J.; Yin, Y.; Liu, E.; Ma, Y.; Wan, J.; Fan, J.; Hu, X. In situ growing Bi_2MoO_6 on g-C_3N_4 nanosheets with enhanced photocatalytic hydrogen evolution and disinfection of bacteria under visible light irradiation. *J. Hazard. Mater.* **2017**, *321*, 183–192. [CrossRef] [PubMed]
12. Zhou, K.; Lu, J.; Yan, Y.; Zhang, C.; Qiu, Y.; Li, W. Highly efficient photocatalytic performance of BiI/Bi_2WO_6 for degradation of tetracycline hydrochloride in an aqueous phase. *RSC Adv.* **2020**, *10*, 12068–12077. [CrossRef]
13. Fu, H.; Pan, C.; Yao, W.; Zhu, Y. Visible-light-induced degradation of rhodamine B by nanosized Bi_2WO_6. *J. Phys. Chem. B* **2005**, *109*, 22432–22439. [CrossRef] [PubMed]
14. Zhang, H.; Yu, D.; Wang, W.; Gao, P.; Bu, K.; Zhang, L.; Zhong, S.; Liu, B. Multiple heterojunction system of $Bi_2MoO_6/WO_3/Ag_3PO_4$ with enhanced visible-light photocatalytic performance towards dye degradation. *Adv. Powder Technol.* **2019**, *30*, 1910–1919. [CrossRef]
15. Huang, D.; Li, J.; Zeng, G.; Xue, W.; Chen, S.; Li, Z.; Deng, R.; Yang, Y.; Cheng, M. Facile construction of hierarchical flower-like Z-scheme AgBr/Bi_2WO_6 photocatalysts for effective removal of tetracycline: Degradation pathways and mechanism. *Chem. Eng. J.* **2019**, *375*, 121991. [CrossRef]
16. Vesali-Kermani, E.; Habibi-Yangjeh, A.; Diarmand-Khalilabad, H.; Ghosh, S. Nitrogen photofixation ability of g-C_3N_4 nanosheets/Bi_2MoO_6 heterojunction photocatalyst under visible-light illumination. *J. Colloid Interf. Sci.* **2020**, *563*, 81–91. [CrossRef] [PubMed]
17. Li, J.; Zhao, Y.; Xia, M.; An, H.; Bai, H.; Wei, J.; Yang, B.; Yang, G. Highly efficient charge transfer at 2D/2D layered P-$La_2Ti_2O_7/Bi_2WO_6$ contact heterojunctions for upgraded visible-light-driven photocatalysis. *Appl. Catal. B-Environ.* **2020**, *261*, 118244. [CrossRef]
18. Zhang, G.; Chen, D.; Li, N.; Xu, Q.; Li, H.; He, J.; Lu, J. Fabrication of Bi_2MoO_6/ZnO hierarchical heterostructures with enhanced visible-light photocatalytic activity. *Appl. Catal. B-Environ.* **2019**, *250*, 313–324. [CrossRef]
19. Zhen, Y.; Yang, C.; Shen, H.; Xue, W.; Gu, C.; Feng, J.; Zhang, Y.; Fu, F.; Liang, Y. Photocatalytic performance and mechanism insights of a S-scheme g-C_3N_4/Bi_2MoO_6 heterostructure in phenol degradation and hydrogen evolution reactions under visible light. *Phys. Chem. Chem. Phys.* **2020**, *22*, 26278–26288. [CrossRef] [PubMed]
20. Zhang, L.; Yang, C.; Lv, K.; Lu, Y.; Li, Q.; Wu, X.; Li, Y.; Li, X.; Fan, J.; Li, M. SPR effect of bismuth enhanced visible photoreactivity of Bi_2WO_6 for NO abatement. *Chin. J. Catal.* **2019**, *40*, 755–764. [CrossRef]
21. Ji, L.; Liu, B.; Qian, Y.; Yang, Q.; Gao, P. Enhanced visible-light-induced photocatalytic disinfection of Escherichia coli by ternary Bi_2WO_6/TiO_2/reduced graphene oxide composite materials: Insight into the underlying mechanism. *Adv. Powder Technol.* **2020**, *31*, 128–138. [CrossRef]
22. Jiang, Y.; Huang, K.; Ling, W.; Wei, X.; Wang, Y.; Wang, J. Investigation of the Kinetics and Reaction Mechanism for Photodegradation Tetracycline Antibiotics over Sulfur-Doped $Bi_2WO_{6-x}/ZnIn_2S_4$ Direct Z-Scheme Heterojunction. *Nanomaterials* **2021**, *11*, 2123. [CrossRef] [PubMed]
23. Alfaro, S.O.; la Cruz, A.M. Synthesis, characterization and visible-light photocatalytic properties of Bi_2WO_6 and $Bi_2W_2O_9$ obtained by co-precipitation method. *Appl. Catal. A Gen.* **2010**, *383*, 128–133. [CrossRef]
24. Wang, D.W.; Siame, B.; Zhang, S.Y.; Wang, G.; Ju, X.S.; Li, J.L.; Lu, Z.L.; Vardaxoglou, Y.; Whittow, W.; Cadman, D.; et al. Direct integration of cold sintered, temperature-stable $Bi_2Mo_2O_9$-K_2MoO_4 ceramics on printed circuit boards for satellite navigation antennas. *J. Eur. Ceram. Soc.* **2020**, *40*, 4029–4034. [CrossRef]
25. Zhang, L.; Xu, T.; Zhao, X.; Zhu, Y. Controllable synthesis of Bi_2MoO_6 and effect of morphology and variation in local structure on photocatalytic activities. *Appl. Catal. B Environ.* **2010**, *98*, 138–146. [CrossRef]
26. Huang, J.; Tan, G.; Ren, H.; Yang, W.; Xu, C.; Zhao, C.; Xia, A. Photoelectric Activity of a Bi_2O_3/Bi_2WO_{6-x} F_{2x} Heterojunction Prepared by a Simple One-Step Microwave Hydrothermal Method. *ACS Appl. Mater. Interfaces* **2014**, *6*, 21041–21050. [CrossRef]
27. Song, J.; Zhang, L.; Yang, J.; Huang, X.; Hu, J. Facile hydrothermal synthesis of Fe^{3+} doped $Bi_2Mo_2O_9$ ultrathin nanosheet with improved photocatalytic performance. *Ceram. Int.* **2017**, *43*, 9214–9219. [CrossRef]
28. Liu, Y.; Chen, J.; Zhang, J.; Tang, Z.; Li, H.; Yuan, J. Z-scheme $BiVO_4$/Ag/Ag_2S composites with enhanced photocatalytic efficiency under visible light. *RSC Adv.* **2020**, *10*, 30245–30253. [CrossRef]
29. He, G.; Zhang, J.; Hu, Y.; Bai, Z.; Wei, C. Dual-template synthesis of mesoporous TiO_2 nanotubes with structure-enhanced functional photocatalytic performance. *Appl. Catal. B-Environ.* **2019**, *250*, 301–312. [CrossRef]
30. Zhang, H.; He, J.; Zhai, C.; Zhu, M. 2D Bi_2WO_6/MoS_2 as a new photo-activated carrier for boosting electrocatalytic methanol oxidation with visible light illumination. *Chin. Chem. Lett.* **2019**, *30*, 2338–2342. [CrossRef]
31. Wang, F.; Li, W.; Gu, S.; Li, H.; Wu, X.; Ren, C.; Liu, X. Facile fabrication of direct Z-scheme MoS2/Bi2WO6 heterojunction photocatalyst with superior photocatalytic performance under visible light irradiation. *J. Photoch. Photobiol. A* **2017**, *335*, 140–148. [CrossRef]

32. Ren, J.; Wang, W.Z.; Sun, S.M.; Zhang, L.; Chang, J. Enhanced photocatalytic activity of Bi_2WO_6 loaded with Ag nanoparticles under visible light irradiation. *Appl. Catal. B-Environ.* **2009**, *92*, 50–55. [CrossRef]
33. Zhang, M.; Du, H.; Ji, J.; Li, F.; Lin, Y.C.; Qin, C.; Zhang, Z.; Shen, Y. Highly Efficient Ag_3PO_4/g-C_3N_4 Z-Scheme Photocatalyst for its Enhanced Photocatalytic Performance in Degradation of Rhodamine B and Phenol. *Molecules* **2021**, *26*, 2062. [CrossRef] [PubMed]
34. Lu, C.; Guo, F.; Yan, Q.; Zhang, Z.; Li, D.; Wang, L.; Zhou, Y. Hydrothermal synthesis of type II $ZnIn_2$S4/$BiPO_4$ heterojunction photocatalyst with dandelion-like microflower structure for enhanced photocatalytic degradation of tetracycline under simulated solar light. *J. Alloys Compd.* **2019**, *811*, 151976. [CrossRef]
35. Singla, S.; Sharma, S.; Basu, S. MoS_2/WO_3 heterojunction with the intensified photocatalytic performance for decomposition of organic pollutants under the broad array of solar light. *J. Clean. Prod.* **2021**, *324*, 129290. [CrossRef]
36. Feizpoor, S.; Habibi-Yangjeh, A.; Ahadzadeh, I.; Yubuta, K. Oxygen-rich TiO_2 decorated with C-Dots: Highly efficient visible-light-responsive photocatalysts in degradations of different contaminants. *Adv. Powder Technol.* **2019**, *30*, 1183–1196. [CrossRef]
37. Zhu, Q.; Sun, Y.; Xu, S.; Li, Y.; Lin, X.; Qin, Y. Rational design of 3D/2D In_2O_3 nanocube/$ZnIn_2S_4$ nanosheet heterojunction photocatalyst with large-area "high-speed channels" for photocatalytic oxidation of 2, 4-dichlorophenol under visible light. *J. Hazard. Mater.* **2020**, *382*, 121098. [CrossRef]
38. Yu, B.; Meng, F.; Khan, M.W.; Qin, R.; Liu, X. Facile synthesis of AgNPs modified TiO_2@ g-C_3N_4 heterojunction composites with enhanced photocatalytic activity under simulated sunlight. *Mater. Res. Bull.* **2020**, *121*, 110641. [CrossRef]
39. Wang, F.; Gu, S.; Shang, R.; Jing, P.; Wang, Y.; Li, W. Fabrication of AgBr/$La_2Ti_2O_7$ hierarchical heterojunctions: Boosted interfacial charge transfer and high efficiency visible-light photocatalytic activity. *Sep. Purif. Technol.* **2019**, *229*, 115798. [CrossRef]
40. Wang, F.; Li, W.; Gu, S.; Li, H.; Liu, X.; Wang, M. Fabrication of $FeWO_4$@$ZnWO_4$/ZnO heterojunction photocatalyst: Synergistic effect of $ZnWO_4$/ZnO and $FeWO_4$@$ZnWO_4$/ZnO heterojunction structure on the enhancement of visible-light photocatalytic activity. *ACS Sustain. Chem. Eng.* **2016**, *4*, 6288–6298. [CrossRef]
41. Sun, X.; Li, H.J.; Ou, N.; Lyu, B.; Gui, B.; Tian, S.; Qian, D.; Wang, X.; Yang, J. Visible-light driven TiO_2 photocatalyst coated with graphene quantum dots of tunable nitrogen doping. *Molecules* **2019**, *24*, 344. [CrossRef] [PubMed]